Fusion Engineering and Design 200 (2024) 114216

Contents lists available at ScienceDirect

Fusion Engineering and Design

journal homepage: www.elsevier.com/locate/fusengdes

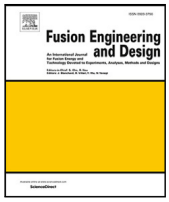

A multi-region and a multiphase MHD OpenFOAM solver for fusion reactor analysis

Simone Siriano *, Lorenzo Melchiorri, Sonia Pignatiello, Alessandro Tassone

Nuclear Engineering Research Group, DIAEE - Sapienza University of Rome, C.so Vittorio Emanuele II 244, 00186 Rm, Rome, Italy

ARTICLE INFO

Keywords:
CFD
Conjugated electric potential
Liquid metal
MHD
OpenFOAM

ABSTRACT

Several systems in nuclear fusion reactors utilize liquid metals as working fluids and the design of these systems cannot overlook the magnetohydrodynamics effects arising from the interaction between the electrically conductive fluid and the magnetic fields used to confine the plasma, since these effects significantly influence the flow features. In this context, rigorous studies and research activities are imperative to provide high–quality numerical data and develop precise predictive numerical tools. This work introduces two OpenFOAM magnetohydrodynamics solvers and outlines their respective validation processes. The `mMRF` solver can simulate single–phase, incompressible MHD flow for multiple electro–coupled domains.

Meanwhile, the `mIF` solver is capable of simulating two–phase MHD flow involving incompressible and immiscible fluids. The `mMRF` solver has demonstrated outstanding results in simulating classical 2D benchmarks up to high magnetic field intensities, while the `mIF` solver proved its ability by estimating, with a discrepancy of less than 10 %, the velocity of a bubble rising within a liquid metal under an imposed magnetic field.

1. Introduction

Liquid Metals (LM), due to their potential to be used both as coolants and tritium breeders, are considered as working fluids in several Breeding Blanket (BB) concepts, such as the Water–Cooled Lead Lithium BB [1], and in advanced concept of Plasma–Facing Components (PFC) [2]. One of the major drawbacks of employing electrically conductive fluids in a system like a magnetic confined fusion reactor is their interaction with the magnetic field, leading to the emergence of magnetohydrodynamic effects (MHD).

Indeed, the induced Lorentz force within the liquid metal changes the flow features with a significant modification of velocity distribution, an increase in pressure losses and generally resulting in the degradation of mass and energy transport processes [3]. For these reasons, the design of these components necessarily requires the development of accurate predictive numerical tools and the production of high–quality numerical data.

In particular, in the context here presented, we are specifically discussing the magnetohydrodynamics of liquid metals (LM–MHD). This is because the characteristic parameters of the LMs and the very intense magnetic field in a reactor allow us to almost always neglect the magnetic field induced by the currents generated in the LM and so the flow has no effect on the distribution of the magnetic field, which is thus imposed from the outside [3]. This leads to the so–called low–magnetic Reynolds approximation where the electric potential can be used as a fundamental quantity to study MHD phenomena with good accuracy [4].

The application of computational methods for solving LM–MHD flows dates back to pioneering analyses in the 70 s and matured towards the 90 s when the increase in computational power allowed considering increasingly stronger magnetic field intensities. This parameter, represented by the Hartmann number (Ha), has a significant impact on the complexity of the analysis. A turning point occurred in 2007 when numerical methods were developed by Ni et al. [4] that significantly accelerated the maximum achievable Hartmann number, reaching 10^4, which is the order of magnitude expected in the next generation of fusion power plants.

Since then, a significant increase in the available tools for simulating LM–MHD flows has been witnessed across all the spectrum from in–house research codes tailored to specific applications to more general purpose computational fluid dynamics (CFD) software, both commercial and open source. A crucial aspect in the development of these tools is the Verification and Validation (V&V) process and for this reason, in 2015, the fusion community agreed upon a series of "baseline" benchmarks to be performed for a rigorous assessment of the tool capabilities [5]. It should be mentioned that the benchmark activities

* Corresponding author.
E-mail address: simone.siriano@uniroma1.it (S. Siriano).

https://doi.org/10.1016/j.fusengdes.2024.114216
Received 13 October 2023; Received in revised form 9 January 2024; Accepted 30 January 2024
Available online 8 February 2024

described, despite covering several different scenarios, are lacking any proposals for multiphase MHD flows; a class of flows relevant for both BB and PFC using LM as working fluids.

In this work, two numerical solvers developed by the Nuclear Engineering Research Group (NERG) of Sapienza University of Rome using the OpenFOAM (OF) open source CFD toolbox are presented along with their validation. In the last 15 years, OF has been a popular choice for the development of LM–MHD tools both for nuclear and non–nuclear applications. Indeed, the possibility of working directly on the source code and exploiting high–performance computing resources without incurring large licensing costs is undoubtedly a great advantage.

A comprehensive review is out of the scope of this paper, but the authors would like to mention some relevant papers that specifically address the simulation of LM–MHD flow at high magnetic field intensity. Arguably, the key development in modeling LM–MHD flow with OF is the work by Dousset [6] from Coventry University in 2009, which develop the tools and investigates MHD flow past a truncated square cylinder. In 2011, Mistrangelo et al. [7] from the Karlsruhe Institute of Technology (KIT) developed and validated up to a high Hartmann number probably the first OF LM–MHD solver. In the same years, a version was also developed by Mas de les Valls et al. [8] from the Universitat Politecnica de Catalunya (UPC), with formal validation up to a Hartmann number of 15 000 conducted more recently in 2022 by Suarez et al. [9] from the same research group. For completeness, it is worth mentioning the version from Delft University of Technology (TU Delft), developed and validated with various cases by Blishchik et al. [10] in 2021, considering also multiphase flow.

The first of the presented solvers is `mhdMultiRegionFoam` (`mMRF`), capable of simulating single–phase, transient, incompressible, isothermal LM–MHD flows. It can handle an arbitrary number of fluid and solid computational domains. The second one is the `mhdInterFoam` (`mIF`) solver, designed for the study of multiphase LM–MHD flows in BB and PFC.

2. MHD numerical model description

2.1. Physical model and discretization

Before presenting the developed tools and their validation, this section outlines the assumptions and the implemented equations common to both the solvers. Homogeneous and isotropic continuous media are considered for both fluid and solid domains. The fluid domains are assumed to be Newtonian and incompressible. The displacement electric current is neglected (low–frequency approximation), as well as the accumulation of electric charge (quasi–neutral approximation) and the induced magnetic field (low–magnetic Reynolds approximation) [11].

With these assumptions and considering the electric potential ϕ as the main electrical variable, a magneto–hydraulic LM–MHD flow (MHD with no heat transfer) is described by the following set of equations, derived from the coupling of the Navier–Stokes', Maxwell's, and Ohm's equations:

$$\nabla \cdot \boldsymbol{u} = 0 \tag{1}$$

$$\rho \left[\frac{\partial \boldsymbol{u}}{\partial t} + (\boldsymbol{u} \cdot \nabla)\, \boldsymbol{u} \right] = -\nabla p + \rho \nu \nabla^2 \boldsymbol{u} + \boldsymbol{j} \times \boldsymbol{B_0} \tag{2}$$

$$\nabla^2 \phi = \nabla \cdot (\boldsymbol{u} \times \boldsymbol{B_0}) \tag{3}$$

$$\boldsymbol{j} = \sigma_F(-\nabla \phi + \boldsymbol{u} \times \boldsymbol{B_0}) \tag{4}$$

where $\boldsymbol{u}$ is the velocity, p the pressure, $\boldsymbol{j}$ the electric current density, $\boldsymbol{B_0}$ the imposed magnetic field, ρ the density, ν the kinematic viscosity and σ_F the electrical conductivity of the fluid.

The dimensionless parameters that completely describe a magneto–hydraulic flow under the proposed assumptions include: the Reynolds number $\mathrm{Re} = u_0 L/\nu$ which represents the ratio between inertial and viscous forces, the interaction parameter (or Stuart number) $\mathrm{N} = \sigma_F {B_0}^2 L/(\rho u_0)$ which represents the ratio between electromagnetic and inertial forces, and the Hartmann number $\mathrm{Ha} = \sqrt{\mathrm{NRe}} = L B_0 \sqrt{\sigma_F/(\rho\nu)}$ which is the square root of the ratio between electromagnetic and viscous forces, where u_0 and L are the mean velocity and the characteristic length. Another important parameter is the wall conductance ratio $c_w = \sigma_S t/(\sigma_F L)$ which represent the ratio between the electrical conductance of the fluid and the solid walls containing it, where σ_S is the electrical conductivity of the wall and t its thickness.

As seen from Eq. (2), the MHD effect is modeled with the inclusion of the Lorentz force ($\boldsymbol{j} \times \boldsymbol{B_0}$) in the momentum equation, which is a volumetric force in a non–conservative form. This means that, using a discretization method that should ensure conservation, such as the Finite Volume Method (FVM) employed in OF, momentum conservation may still not be guaranteed if the equation is discretized in this form and without any particular precautions. Indeed, by substituting the current density with Ohm's law (Eq. (4)) and discretizing, the term $\boldsymbol{u} \times \boldsymbol{B_0}$ is not derived from the fluxes of quantities on the faces of the Control Volume (CV), but directly from the values of velocity and magnetic field at the center of the CV. This is implied in the discretization of the Ohm's equation itself if it is performed without specific adjustments, and it implies that the conservation of charge and momentum, when it should be as in the Shercliff flow, is not guaranteed, as demonstrate in [4].

Ni et al. [4] propose two techniques to conservatively calculate the Lorentz force on an arbitrary collocated mesh:

1. Based on a conservative interpolation scheme of the current density at the cell center from the cell faces of a CV, value that will be use for the calculation of the Lorentz force.
2. Based on a conservative formulation of the Lorentz force that does not require evaluating the electric current density at the center of the CV but only the current density fluxes on the faces of the CV. Obviously this eliminate the numerical error from the interpolation to get the CV center values of the current. Another advantage is that this formulation can also be used in the presence of a non–uniform magnetic field.

In the solvers presented below, the second one of these proposed technique has been adopted, in which the discretized Lorentz force is expressed by this conservative formula:

$$\begin{aligned}(\boldsymbol{j} \times \boldsymbol{B_0})_c = &- \frac{1}{V_{CV}} \left[\sum_{f=1}^{n_f} (J_n)_f (\boldsymbol{B_0} \times \boldsymbol{r}_c)_f \right] + \\ &- \frac{1}{V_{CV}} \left[\boldsymbol{r}_c \times \sum_{f=1}^{n_f} (J_n)_f (\boldsymbol{B_0})_f s_f \right],\end{aligned} \tag{5}$$

where the subscript c denotes the CV center value, the one f the face center value, V_{CV} is the volume of the CV, s_f is the area of the cell face, nf is the number of faces which constitute the CV, $\boldsymbol{r}_c$ in the center of CV coordinate and, finally, $(J_n)_f$ is the current density flux on the faces of the CV.

The critical part is the evaluation of $(J_n)_f$ that must be carried out with a conservative scheme which ensure $\sum_{f=1}^{n_f} (J_n)_f s_f = 0$ close to machine precision. The $(J_n)_f$ is computed by the Ohm's law, with the following discretized formula

$$(J_n)_f = \sigma_F \left[-\left(\frac{\partial \phi_c}{\partial n} \right)_f + (\boldsymbol{u} \times \boldsymbol{B_0})_f \cdot \boldsymbol{n}_f \right], \tag{6}$$

which needs the center CV value of the electric potential, derived from the iterative resolution of the electric potential Poisson equation

$$\sum_{f=1}^{n_f} \sigma_F \left(\frac{\partial \phi_c}{\partial n} \right)_f s_f = \sum_{f=1}^{n_f} \sigma_F (\boldsymbol{u} \times \boldsymbol{B_0})_f \cdot \boldsymbol{n}_f s_f \tag{7}$$

The key point highlighted by Ni et al. [4] is that the $\partial \phi_c/\partial n$ must be discretized with the same scheme and must consider a correction

for non–orthogonality to ensure charge conservation for non–structured meshes, that is

$$\left(\frac{\partial \phi_c}{\partial n}\right)_f = \underbrace{f_1\left(\phi_c\right)}_{\text{orthogonal}} + \underbrace{f_2\left(\phi_c, \nabla\phi_c\right)}_{\text{non–orthogonal}} \tag{8}$$

with $\nabla\phi_c$ evaluated with the Gauss' rule

$$\nabla\phi_c = \frac{1}{V_{CV}} \sum_{f=1}^{n_f} \phi_f s_f \boldsymbol{n}_f \tag{9}$$

They proposed two discretization formulas that include a correction for non–orthogonality [4]. However, in the solvers presented below, the scheme already existing in OF was used, which represents the gradient with an orthogonal term calculated implicitly and a non–orthogonal correction term calculated explicitly [12].

2.2. MHD code workflow

In this section, the calculation algorithm of the MHD model presented above is briefly described, omitting the hydrodynamic computation part, which is performed using the PIMPLE[1] algorithm. For a detailed description of the hydrodynamic computation, please refer to the provided Ref. [12].

1. Initial mapping of the fields ($\boldsymbol{u}$, p, phi, etc.) from imposed initial conditions, evaluation for $t = 0$ of the Lorentz force using Eq. (5).
2. PIMPLE algorithm for time t, converged values of $\boldsymbol{u}$ and p.
3. Solving of the electric potential Poisson Eq. (7) for ϕ_c.
4. Calculation of $\partial\phi_c/\partial n$ from Eq. (8) and calculation of $(\boldsymbol{J}_n)_f$ from Eq. (6) with $\nabla\phi_c$ computed from Eq. (9).
5. Calculation of the updated value of the Lorentz force using Eq. (5).
6. Performing of eventual n external PIMPLE loops to improve the coupling between the dynamic and electromagnetic variable.
7. Repeat steps from $2 \div 6$ for $t = t + dT$.

3. The mMRF solver: code description and validation

3.1. Code description

The mhdMultiRegionFoam is a solver capable of simulating time–dependent, incompressible, and isothermal MHD flow in an arbitrary number of fluid and solid regions. The solver is based on the chtMultiRegionFoam solver of OF 9, designed for solving conjugate heat transfer problems involving multiple regions or domains, coupled with an internal Boundary Condition (BC). The strategy for solving the coupled heat transfer is *segregated*, meaning that first, the equations in the fluid domains are solved using the temperature field in the solids from the previous time iteration. Then, the equations for the solids are solved using the temperature field in the fluids from the previous step. This procedure is iteratively repeated until the solution converges, and this iterative process is controlled by the PIMPLE loop setup.

Another coupling strategy is the so-called *grid coupling strategy* which avoids the use of the internal BC by directly coupling the meshes of all domains and solving a unique matrix system. The advantage of this approach is that it eliminates internal iterations between domains, although it requires processing much larger matrices at the solver level [8]. However, the authors have found that three external PIMPLE iterations are sufficient to couple the solution between the fluid and solid domains. This, combined with the lower memory requirements needed to process individual region meshes (instead of a global mesh) and the great flexibility in using internal BC, makes this strategy very promising for integration into a multi–physics platform.

[1] Pressure Implicit Method for Pressure–Linked Equations.

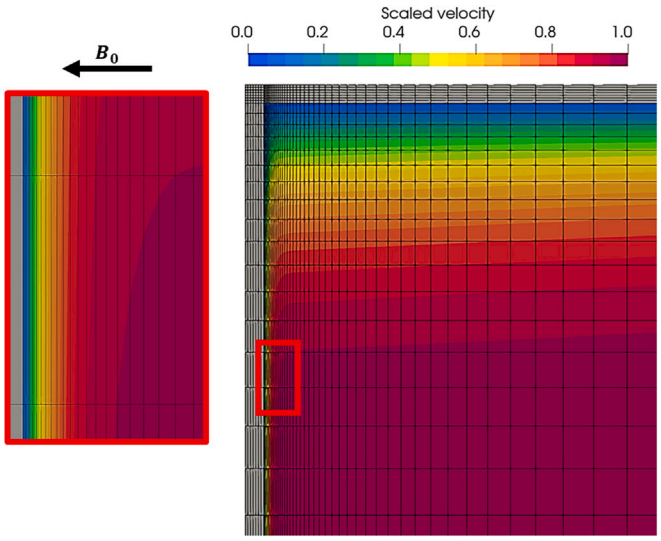

Fig. 1. Computational grid on the channel cross–section for the Shercliff flow at Ha = 500. Detail of the nodes distribution through the side layer (wall parallel to $\boldsymbol{B}_0$) and through the Hartmann layer (left box, wall perpendicular to $\boldsymbol{B}_0$). The scaled velocity is the ratio between the axial velocity and the value of the axial velocity at the center of the outlet channel cross–section.

However, regardless of the strategy employed, the transport equations between domains need to be coupled, conserving the main variable at the interface among the regions. In the case of the mMRF solver, the coupling BC has been modified to ensure the continuity of the electric potential and the conservation of its flux (or electric current) at the interface, implementing the following equations, where the subscript F and S mean, respectively, fluid and solid:

$$\phi_F = \phi_S \tag{10}$$

$$\sigma_F \frac{\partial \phi_F}{\partial n} = -\sigma_S \frac{\partial \phi_S}{\partial n} \tag{11}$$

Therefore, considering the workflow presented in Section 2.2, the steps executed in the code are the same but with the following differences:

1. After step 5, $\phi_{c,S}$ and $\partial\phi_{c,S}/\partial n$ in solids are calculated respectively with Eqs. (7) and (6), considering that $\boldsymbol{u} = 0$ and that the electrical conductivity is that of the respective solid region under consideration.
2. Step 6 becomes crucial to ensure the coherence of the electric potential field between fluids and solids. Usually, three external PIMPLE cycles are sufficient to guarantee this coherence.

3.2. Validation

This section will present the results for the baseline benchmark problem as outlined in the Ref. [5], which consist simulating a fully developed (2D), laminar, steady MHD flow within a square duct subjected to a uniform transverse magnetic field $\boldsymbol{B}_0$, up to high Hartmann numbers. Two distinct wall electrical conductivity conditions were explored: one with perfectly electrically insulated walls ($c_w = 0$), corresponding to the Shercliff flow and labeled as A1 in the benchmark, and another with perfectly insulated side walls (parallel to $\boldsymbol{B}_0$) and electrically conductive ($c_w = 0.01$) Hartmann walls (perpendicular to $\boldsymbol{B}_0$), corresponding to the Hunt flow, labeled as A2. Explanation of physical phenomena and discussion of flows features for these classical MHD flows can be found in established MHD literature, such as the Ref. [3].

The numerical domain consist a half–square, where, to reduce computational effort, the symmetry boundary condition was applied on

the symmetry plane perpendicular to $\boldsymbol{B_0}$. An uniform pressure value of zero was enforced at the outlet, along with the `zeroGradient` BC for velocity, ensuring a fully developed flow. At the inlet, the `zeroGradient` BC for pressure was applied, and the velocity was mapped through the `mapped` BC, which connects the inlet and outlet, ensuring a fixed value of mean velocity on the cross–section. This approach effectively models an infinitely long channel simulating only a small axial length. At the fluid–solid interface, the `zeroGradient` BC and the `noSlip` BC were set for pressure and velocity, respectively, and the custom coupling boundary condition ensured the continuity of electric potential and conservation of current density. Regarding the electric potential, the `zeroGradient` BC was applied at the inlet and outlet, following the expected 2D current distribution, as well as at the external boundary of the walls.

The governing equations were solved on a structured, hexahedral and coherent mesh, with higher resolution near the walls where the MHD boundary layers develop, as shown in Fig. 1. For all the analyzed cases, 7 elements were placed inside the wall thickness and 9 elements were positioned between the inlet and outlet. It was observed that the `mapped` BC is sensitive to the number of axial elements, making it possibly not the most optimal solution for achieving periodicity between two patches. The exploration of alternative boundary conditions for this purpose is still under analysis.

A second–order `backward` discretization scheme was employed for the temporal term, while Gauss discretization with linear interpolation of variables was applied to all other terms. Concerning the resolution of the discretized equations, the PCG.[2] method with the DIC[3] preconditioner was utilized for the pressure and electric potential variables, whereas the PBiCGStab[4] method with the DILU[5] preconditioner was applied to the velocity variable [12]. As previously stated, PIMPLE algorithm was employed for the pressure–velocity coupling, performing two internal corrector loops and a minimum of three external loops. Convergence of the simulations was deemed achieved when the residuals of all variables reached values below 10^{-6} and the discrepancy of select physically significant variables between consecutive iterations $((x^t - x^{t-1})/x^{t-1})$ fell below 10^{-6}.

The benchmark involves comparing the numerical dimensionless flow rate Q^*_{OF} with the analytical values Q^*_{AN} provided in Ref. [5]. It is important to underline that these analytical solutions are valid considering the so-called *thin–wall* condition [3]. Therefore, a ratio between the characteristic length L, i.e the half–length of the side parallel to $\boldsymbol{B_0}$, and wall thickness t equal to 10^{-2} was considered. The relation to calculate the dimensionless flow rate are:

$$Q^* = \int_{-1}^{1} dy^* \int_{-1}^{1} U^* dz^* \tag{12}$$

$$U^* = \frac{U}{\left[L^2(-dP/dx)/(\nu\rho)\right]} \tag{13}$$

where U represents the integral area average value computed at the outlet of the numerical domain and the pressure gradient dP/dx is calculated as the ratio of the pressure drop (the integral area average value at the inlet due to the fixed zero–value at the outlet) and the axial length of the domain.

A mesh sensitivity analysis was conducted for both the A1 and A2 cases at Ha = 500, aiming to investigate the influence of resolution on both the Hartmann Layer (HL) and the Side Layer (SL). The HL develops on the Hartmann wall and its thickness scales with $\sim L/\mathrm{Ha}$, while the SL develops on the side walls and scales with $\sim L/\sqrt{\mathrm{Ha}}$.

In addition to considering the integral quantity Q^* as a comparison parameter through the error $E(Q^*) = |Q^*_{OF} - Q^*_{AN}|/Q^*_{AN}$, two local quantities are also taken into account. Specifically, axial velocity (u_x) profiles were examined on the two principal axes of the channel cross–section: one in the z–direction, parallel to $\boldsymbol{B_0}$, passing through the HL denoted as I_{HP}, and the other in the y–direction, perpendicular to $\boldsymbol{B_0}$, passing through the SL denoted as I_{SP}. Discrepancies between the numerical and analytical integral values were computed in an absolute discrete manner, avoiding compensations of velocity excess in some parts of the profile with defects in other parts. This was achieved utilizing the formula $E(I_x) = \sum_{i=1}^{sp} |I_{x,OF} - I_{x,AN}| / \sum_{i=1}^{sp} I_{x,AN}$, with sp the number of sampling points.

Table 1
Results of the mesh sensitivity analysis for the A1 case with Ha = 500.

HL division	SL division	Number of elements	$E(Q^*)$ (%)	$E(I_{HP})$ (%)	$E(I_{SP})$ (%)
0	6	30 096	25.14	0.722	1.258
2	6	38 304	3.280	0.049	0.173
4	6	44 460	0.957	0.043	0.117
6	6	47 880	0.602	0.041	0.115
8	6	50 616	0.468	0.038	0.115
10	6	52 668	0.395	0.033	0.105
6	8	52 920	0.585	0.029	0.102
6	10	56 700	0.577	0.022	0.096
6	12	60 480	0.571	0.018	0.092

Table 2
Results of the mesh sensitivity analysis for the A2 case with Ha = 500.

HL division	SL division	Number of elements	$E(Q^*)$ (%)	$E(I_{HP})$ (%)	$E(I_{SP})$ (%)
0	6	30 096	3.846	0.730	0.830
2	6	38 304	1.008	0.282	0.378
4	6	44 460	0.638	0.267	0.362
6	6	47 880	0.576	0.255	0.361
8	6	50 616	0.550	0.251	0.359
10	6	52 668	0.526	0.229	0.334
6	8	52 920	0.540	0.216	0.326
6	10	56 700	0.521	0.203	0.311
6	12	60 480	0.510	0.194	0.302

Table 3
Results of the validation process for the A1 case.

Ha	Q^*_{AN}[%]	E(Q*)(%)	$E(I_{HP})$(%)	$E(I_{SP})$(%)
500	7.680×10^{-3}	0.602	0.044	0.115
5000	7.902×10^{-4}	0.424	0.022	0.033
10000	3.965×10^{-4}	0.386	0.040	0.015
15000	2.648×10^{-4}	0.383	0.022	0.065

Table 4
Results of the validation process for the A2 case.

Ha	Q^*_{AN}[%]	E(Q*)(%)	$E(I_{HP})$(%)	$E(I_{SP})$(%)
500	1.405×10^{-3}	0.576	0.255	1.363
5000	1.907×10^{-5}	0.055	0.624	0.620
10000	5.169×10^{-6}	0.018	0.118	0.981
15000	2.425×10^{-6}	0.248	0.036	1.127

The results of the sensitivity analysis for case A1 and A2 are presented in Tables 1 and 2, respectively. Increasing layer resolution generally reduces discrepancies with reference quantities, but HL resolution impacts the solution more than SL. For A1, < 4 divisions of HL cause significant errors due to current leakage, leading to underestimated Lorentz force and higher flow rate. A2 allows < 2 elements to maintain < 1% error. The authors concluded that considering 6 elements in both the HL and SL for both cases represents a suitable compromise between accuracy and computational cost for the continuation of the validation activity.

Tables 3 and 4 present the validation results for the A1 and A2 cases, respectively. The numerical results exhibit an excellent agreement with the analytical solutions across all tested magnetic field intensities for

[2] Preconditioned Conjugate Gradient.
[3] Simplified Diagonal–based Incomplete Cholesky.
[4] Preconditioned Bi–Conjugate Gradient Stabilized.
[5] Simplified Diagonal–based Incomplete LU.

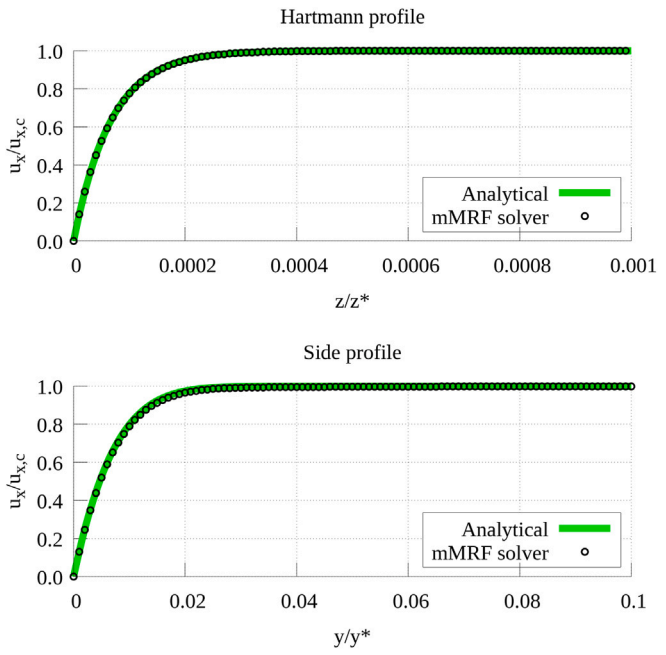

Fig. 2. Dimensionless velocity profiles near the Hartmann (up) and side (down) layer for the A1 case for Ha = 15 000. The scale velocity $u_{x,C}$ si the velocity at the center of the cross–section.

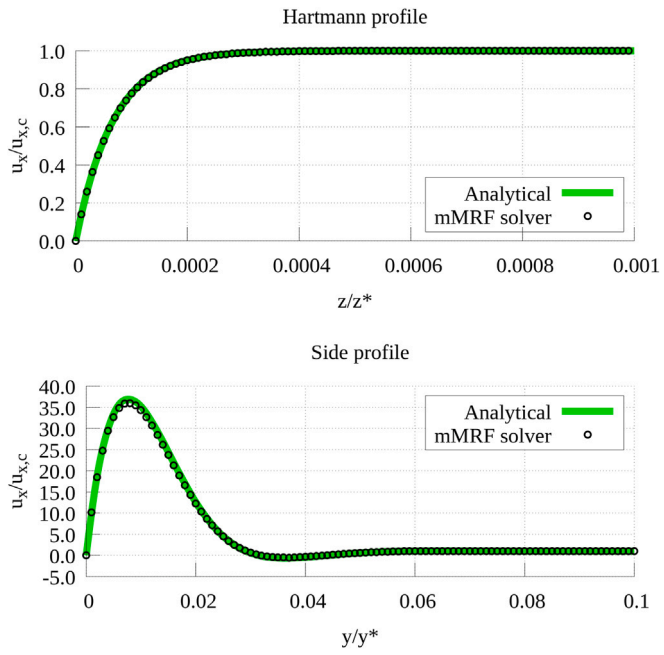

Fig. 3. Dimensionless velocity profiles near the Hartmann (up) and side (down) layer for the A2 case for Ha = 15 000. The scale velocity $u_{x,C}$ si the velocity at the center of the cross–section.

both cases, with a maximum deviation of approximately 1%. This high level of accuracy is further evident in the comparison between the numerical and analytical velocity profiles [4] along the main cross–section axis in the z and y–directions.

Figs. 2 and 3 depict these comparisons for the A1 and A2 flows, respectively, showcasing the robustness of the numerical simulations, especially in the most challenging case.

4. The mIF solver: code description and validation

4.1. Code description

The mhdInterFoam is a solver capable of carrying out MHD time–dependent simulation of two incompressible, isothermal and immiscible fluids. Currently, it supports only the fluid region, so it is possible to model only ideal electric wall conditions through BCs, such as perfectly electrically insulated and conductive walls.

The solver is based on the interIsoFoam solver of OF v2212, which is an extension of the interFoam solver using the isoAdvector phase–fraction based interface capturing approach [13], with optional mesh motion and mesh topology changes including adaptive re–meshing. The implementation of MHD effects was carried out by adapting the guidelines from what is arguably the most significant work in numerical modeling of MHD multiphase phenomena, the 2014 study by Zhang et al. [14], to the structure of the base solver.

The solver interIsoFoam has been already tested by the authors under hydrodynamic conditions for an high–density ratio mixture, a potentially critical condition for multiphase numerical models, correctly simulating several flow regime for the rise of helium bubbles within the lead–lithium eutectic alloy [15].

The two–phase modeling is performed employing the Volume of Fluid (VOF) method, a free–surface modeling technique which use a scalar function α that represent the volume fraction of each fluid in a CV. A value equal to 0 indicates that phase 1 is present in that specific CV, while a value equal to 1 means that phase 2 is present in that specific CV. Control volumes with values between these two extremes represent the interface between the two phases. Excluding phase changes, the mass of a certain phase must be conserved, and thus:

$$\frac{\partial \alpha}{\partial t} + \nabla \cdot (\alpha \boldsymbol{u}) = 0 \tag{14}$$

In essence, this represents the advection equation of the interface, and its solution must preserve its sharpness. The interIsoFoam solver provides three different solutions to achieve this, and in the following, the isoAdvector method [13] has been applied. For a detailed description of interIsoFoam refer to Refs. [11,15].

Once the alpha distribution is calculated, material properties are updated within the computational domain according to the following relationship, where β represents a generic property:

$$\beta = \alpha\beta_1 + (1-\alpha)\beta_2 \tag{15}$$

The VOF method employ a single momentum equation for the whole mixture and below is reported the one implemented in the mIF solver, which includes the Lorentz force:

$$\rho\left[\frac{\partial \boldsymbol{u}}{\partial t} + (\boldsymbol{u}\cdot\nabla)\boldsymbol{u}\right] = \\ -\nabla p + \nabla\cdot\boldsymbol{\Psi} + \boldsymbol{F}_S + \rho\boldsymbol{g} + \boldsymbol{j}\times\boldsymbol{B_0} \tag{16}$$

where $\boldsymbol{\Psi}$ is the viscous stress tensor, $\boldsymbol{g}$ the gravitational acceleration and $\boldsymbol{F}_S$ the surface tension which is modeled as a volumetric force employing the Continuum Surface Force (CSF) technique of Brackbill et al. [16]

$$\boldsymbol{F}_S = \gamma\kappa\nabla\alpha \tag{17}$$

$$\kappa = \nabla\cdot\left(\frac{\nabla\alpha}{|\nabla\alpha|}\right) \tag{18}$$

where γ is the surface tension coefficient and κ the interface curvature.

As shown in the previous equations and in the algorithm proposed in [14], MHD effects manifest only in the momentum Eq. (16), where the Lorentz force was calculated using the conservative formula (5) and closure of the equations system was performed using Eqs. (6) and (7), where electrical conductivity is calculated using Eq. (15).

Considering the workflow presented in Section 2.2, it is modified by including the following steps between step 1 and 2:

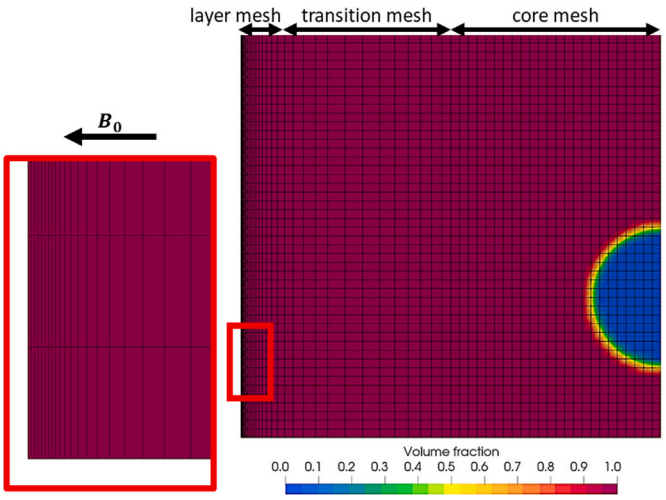

Fig. 4. Computational grid on the bottom part of the midplane cross–section for the bubble with $d = 5.60\,\text{mm}$ and $B_0 = 0.5\,\text{T}$ at time zero. Detail of the nodes distribution through the Hartmann layer (left box).

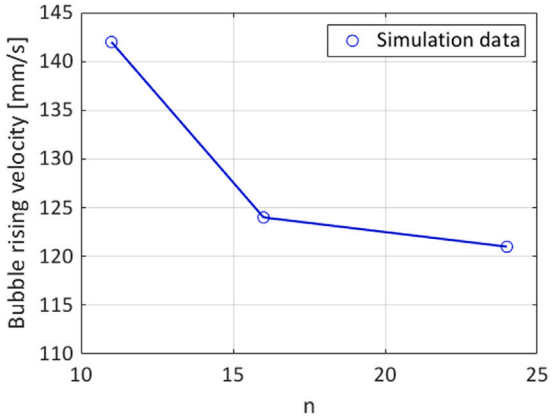

Fig. 5. Results of the mesh sensitivity analysis for the bubble with $d = 5.60\,\text{mm}$ for $B_0 = 1\,\text{T}$. The bubble rising velocity is the time–average value of the terminal velocity up to $0.1\,\text{s}$.

1. Variables are updated due to possible mesh modifications (adaptive re–meshing).
2. The alpha transport Eq. (14) is computed, considering the velocity field from the previous time–step, and thus, the position of the interface between phases is known.
3. Material properties are updated with the new alpha distribution (Eq. (15)).

The remaining steps remain essentially unchanged, where PIMPLE is responsible for the velocity–pressure coupling in the momentum equation and the calculation of the MHD part follows steps 4 and 5.

4.2. Validation

In this section, we present the results of the validation process for the mIF code. This validation involves simulating the rising of a nitrogen bubble in a square channel filled with liquid mercury under the influence of a transversal uniform magnetic field $\boldsymbol{B_0}$. This particular case was previously explored by Mori et al. [17], where the bubble dynamics for various initial diameters d was investigated under three different magnetic field intensities, ranging from 0.5 to 1.5 T.

The parameter chosen for comparison is the terminal velocity of the bubble U_T. Initially at rest, the bubble undergoes acceleration

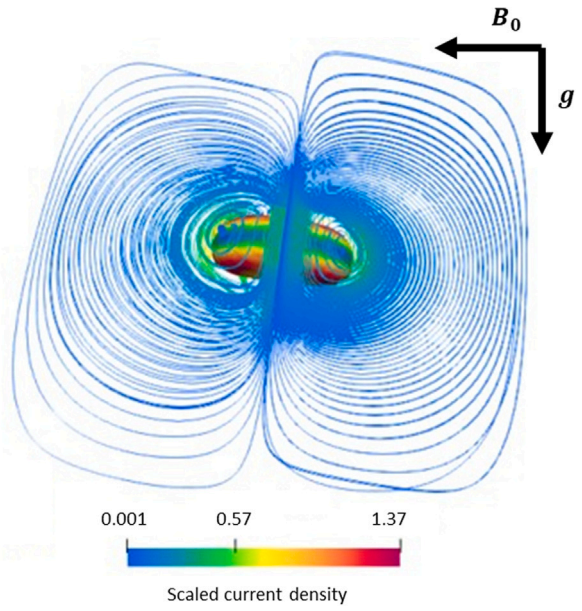

Fig. 6. Electric currents streamlines near the bubble with $d = 5.60\,\text{mm}$ and $B_0 = 0.5\,\text{T}$. The scaled current density is the ratio between the current density magnitude and the characteristic value equal to $\sigma u_T B_0$ with $\sigma = 8.8 \times 10^4\,\text{A m}^{-2}$.

until it attains a limit velocity, a value contingent upon factors such as the bubble diameter, material properties and the intensity of the magnetic field. This terminal velocity, apart from minor oscillations, remains relatively constant. The convergence criteria are established by observing this behavior, deeming the simulation converged when the oscillations remain within the range of $\pm 10\%$ concerning the terminal velocity. Achieving this requires a simulation time–frame between 0.21 and 0.25 s.

Referring to the original paper [17] for a detailed description of the experimental test section, it is crucial to note that producing a perfectly spherical bubble and accurately measuring its diameter and its velocity in an opaque medium like mercury is a challenging task. The bubbles were created by injecting nitrogen through a nozzle and their diameter was estimated based on the nitrogen flow rate and the rate of bubble generation measured using an electrical triple probe system, which is used also for the bubbles velocity. Due to these uncertainties, the authors conducted multiple experiments using the same nitrogen flow rate and determined the rising velocity through a statistical model. Additionally, the probe system allowed for estimating the bubble diameter at the starting point from the point of impact between the bubble and the probes and they observed a discrepancy compared to the initial estimate of about 30 % [17].

The numerical domain is represented as a parallelepiped, with a square base measuring $6d \times 6d$. In general, the magnetic field exerts a significant influence on the velocity, and depending on the bubble's dimensions, the domain height needs to be adjusted to provide an appropriate time–frame and space for computing the terminal velocity. For the considered parameters, the domain height ranges from $16d$ to $42d$.

The motion of the spherical nitrogen bubble start from rest at a distance of $1d$ above the bottom wall considering the bubble centroid, while the liquid mercury remains stationary, with a zero–velocity condition imposed throughout the domain. The material properties considered in this simulation are detailed in the Ref. [18] and the main dimensionless parameter, i.e. the Re or Galilei number, the Eötvös number (ratio between gravitational and surface tension forces) and Ha vary in the interval $3200 \leq \text{Re} \leq 11\,800$, $1.5 \leq \text{Eo} \leq 8.5$ and $0 \leq \text{Ha} \leq 148$.

Concerning the BCs, the noSlip condition for velocity and the zeroGradient condition for pressure, volume fraction and electric potential

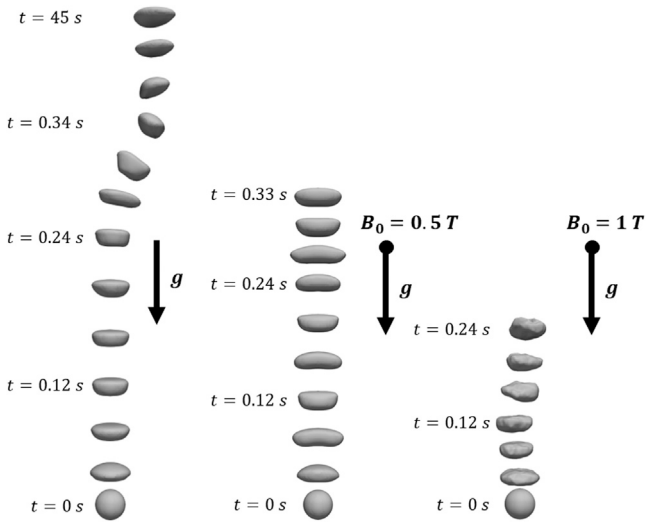

Fig. 7. Shape of the bubble with $d = 5.60\,\mathrm{mm}$ for the hydrodynamic case (left), $B_0 = 0.5\,\mathrm{T}$ (center) and $B_0 = 1\,\mathrm{T}$. The bubble is computed and the isovolume for the value $\alpha = 0.5$ at several time–steps.

have been applied on all walls. This last condition is in line with the glass channel used by Ref. [17].

The generation of a suitable computational grid, ensuring both accuracy and reasonable computational cost, presents a significant challenge in modeling flows of this nature. The presence of a practically perfect electrical insulator, like nitrogen, leads an accumulation of the electric current near the bubble interface, as shown in Fig. 6, resulting in the generation of a MHD layer near the interface. Ensuring a certain level of resolution within these layers implies having a highly refined mesh in all parts of the domain where the bubble rises, which means to an enormous number of mesh elements, or the use of Adaptive Mesh Refinement (AMR) technique capable of automatically refining the mesh near the interface. The `mIF` solver has inherited the capability to employ AMR from the base `interIsoFoam` solver however, as it stands, this approach does not seem suitable for application in an MHD case. Further analyses are currently underway to explore this possibility, and the findings will be discussed in detail in a dedicated future paper.

Currently, the meshing strategy is designed based on a criterion independent of the resolution of the MHD layers near the interface. This approach, in line with proposals in the existing literature [14,18], is primarily founded on the bubble diameter. Specifically, the mesh configuration comprises a core mesh with dimensions $3d \times 3d$, consisting of uniformly sized square elements of $d/n \times d/n$. This core mesh is followed by a transition mesh from the core to the mesh near the walls, where the elements measure $d/8 \times d/8$. Finally, the mesh near the walls is designed to ensure 7 divisions across the MHD layers, as shown in Fig. 4. The parameter n introduced above was determined through a mesh sensitivity analysis, considering values of $n = 11$, $n = 16$ and $n = 24$ and the average value of the terminal velocity up to 0.1 s as a comparing parameter. The analysis revealed a solution independent of mesh resolution for $n = 16$, as shown in Fig. 5, which was consequently chosen for all the cases presented hereafter. The obtained results, along with the employed discretization scheme and algebraic solver, will be comprehensively discussed in a future dedicated paper.

Fig. 8 illustrates the rising velocity of the bubble with a diameter of 5.60 mm moving through a 0.5 T magnetic field. The results from two other codes, taken from Ref. [18] (labeled Code A) and Ref. [14] (Code B), are also presented, alongside the experimental terminal velocity value of $168\,\mathrm{m\,s^{-1}}$ [17]. Both the `mIF` solver and Code A simulate a very short–lived initial phase, extending from 0 to approximately 0.01 s, characterized by the rapid bubble acceleration. Subsequently,

Table 5
Results of the validation. The symbols $U_{T,ex}$ and $U_{T,mIF}$ refer, respectively, to the experimental value in [17] and the `mIF` results.

B_0 (T)	d (mm)	$U_{T,ex}$ (mm/s)	$U_{T,mIF}$ (mm/s)	$E(U_T)(\%)$
0.0	2.36	189	207	9.5
0.0	3.87	192	189	−1.6
0.0	5.60	201	203	1.0
0.5	2.36	199	187	−6.0
0.5	3.87	184	174	−5.4
0.5	5.60	168	172	2.4
1.0	5.60	143	134	−6.3

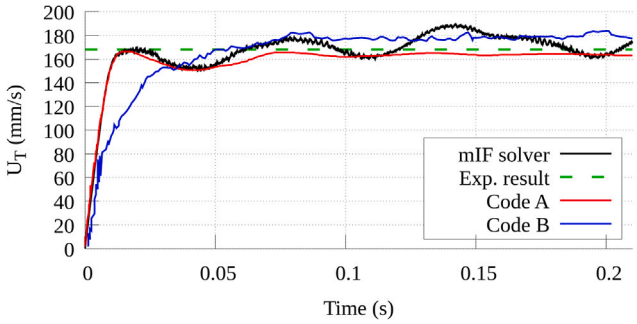

Fig. 8. Rising velocity for the bubble with $d = 5.60\,\mathrm{mm}$ under a magnetic field with intensity 0.5 T. Code A refers to the numerical investigation described in [18], code B to Ref. [14].

the velocity reaches a plateau and begins oscillating around a mean value. Code B also reaches this point, albeit with a smoother initial phase. Across all three codes, the average velocity closely aligns with the experimentally measured value. As shown in Fig. 8, our results exhibit minor oscillations throughout the timeframe compared to other codes. This is likely due to the small time–step used in our simulation, which is on the order of $10^{-5} \div 10^{-6}$, and the fact that we probe the velocity at each time–step.

Table 5 collects the results for all the considered bubbles, demonstrating that the code accurately predicts the terminal velocity of the bubbles, with a maximum discrepancy from the experimental data of approximately 10 %.

It should be noted that the experimental values of the terminal velocity in the absence of magnetic fields exhibit discrepancies, some of which are significant, compared to the Mendelson formula [19], which is commonly used to estimate rising velocity in a hydrodynamic regime. This disparity is likely attributed to the perturbations in the measurement system concerning the motion field of the metal surrounding the bubble. These perturbations could be expected to impact measurements even when the magnetic field is applied. Considering the uncertainties associated with the measured velocity and the starting bubble's shape and diameter, mentioned before, the authors regard the results of the validation activity as successful.

Fig. 7 shows the shape of the bubble during its ascent for several time–steps. As expected due to the small values of the Eötvös and Galilei numbers, the shape of the bubble without the magnetic field is ellipsoidal, without undergoing the creation of filaments or breaking. Considering the magnetic field, there is not a significant change in the shape behavior, where the bubble remains substantially ellipsoidal with the short axis aligned with the magnetic field direction and the long one perpendicular to the magnetic field, as also found in [20]. In this figure, the braking action of the Lorentz force is clearly visible, where the bubble covers a smaller rising space considering the same time–frame, essentially remaining on an almost straight trajectory.

5. Conclusions and future works

In this paper, we introduced two OpenFOAM solvers for computational magnetohydrodynamics developed by the NERG of Sapienza

University of Rome. The first code, the `mhdMultiRegionFoam` solver, has the capability to simulate time–dependent, incompressible, and isothermal MHD flow, accounting for fluid–solid electrical coupling. The code underwent validation through classic 2D benchmarks up to $Ha = 15\,000$, demonstrating outstanding results. In the future, the code will be improved with the implementation of heat transfer and buoyancy effects and will undergo further validation considering the benchmarks described in Ref. [5]. Upon completion of these developments, the code will have the capability to model single–phase magneto–convective flows under relevant fusion conditions.

The second solver, `mhdInterFoam`, is an isothermal, immiscible two–phase MHD tool based on the Volume of Fluid method. In this paper, we present the initial phase of the validation process, involving the modeling of a rising bubble in liquid metal under the influence of a uniform transverse magnetic field. The results are promising, with a discrepancy of less than 10 % compared to the selected experimental validation data. Planning is underway to identify and select suitable benchmarks for other multiphase MHD scenarios. This activity is deemed as a necessary step to integrate the validation protocol outlined in Ref. [5], which currently does not consider any multiphase flow, to cover all the relevant physical scenarios expected in BB and PFC. A preliminary candidate has already been identified for the case of a thin–film flow over an inclined substrate, for which analytical solutions and other numerical results exist to provide a frame of Ref. [21,22].

Furthermore, we ultimately plan to integrate these two solvers into a flexible and comprehensive platform for the simulation of MHD flows in a variety of conditions representative of all those LM systems and components currently under development for fusion reactors. To this end, activities are being planned and are ongoing to extend the capabilities of the existing code base, e.g. simulating the LM compressibility and pressurization during coolant leakage transients [23,24], coupling with a dedicated system thermal–hydraulics code with MHD effects (REDMaHD) [25], transport of tritium and activated corrosion products in the LM [26,27], etc.

CRediT authorship contribution statement

Simone Siriano: Writing – review & editing, Writing – original draft, Visualization, Validation, Software, Methodology, Investigation, Formal analysis, Conceptualization. **Lorenzo Melchiorri:** Writing – review & editing, Visualization, Validation, Investigation, Formal analysis. **Sonia Pignatiello:** Writing – review & editing, Visualization, Validation, Software, Methodology, Investigation, Formal analysis. **Alessandro Tassone:** Writing – review & editing, Supervision, Conceptualization.

Declaration of competing interest

The authors declare that they have no known competing financial interests or personal relationships that could have appeared to influence the work reported in this paper.

Data availability

Data will be made available on request.

Acknowledgments

This work has been carried out within the framework of the EUROfusion Consortium, funded by the European Union via the Euratom Research and Training Programme (Grant Agreement No 101052200 — EUROfusion). Views and opinions expressed are however those of the author(s) only and do not necessarily reflect those of the European Union or the European Commission. Neither the European Union nor the European Commission can be held responsible for them.

The computational resources and the related technical support used for this work have been provided by CRESCO /ENEAGRID High Performance Computing infrastructure and its staff [28]. CRESCO/ENEAGRID High Performance Computing infrastructure is funded by ENEA, the Italian National Agency for New Technologies, Energy and Sustainable Economic Development and by Italian and European research programmes, see www.cresco.enea.it/english for information.

During the preparation of this work, the author(s) used the OpenAI GPT language model, commonly known as ChatGPT, in order to improve the clarity and structure of English writing, as well as to assist with formatting tasks. After using this tool/service, the author(s) reviewed and edited the content as needed and take(s) full responsibility for the content of the publication.

References

[1] P. Arena, G. Bongiovì, I. Catanzaro, C. Ciurluini, A. Collaku, A.D. Nevo, P.A.D. Maio, M. D'Onorio, F. Giannetti, V. Imbriani, P. Maccari, L. Melchiorri, F. Moro, R. Mozzillo, S. Noce, L. Savoldi, S. Siriano, A. Tassone, M. Utili, Design and integration of the EU-DEMO water-cooled lead lithium breeding blanket, Energies 16 (2023) 2069.

[2] C.E. Kessel, D. Andruczyk, J.P. Blanchard, T. Bohm, A. Davis, K. Hollis, P.W. Humrickhouse, M. Hvasta, M. Jaworski, J. Jun, Y. Katoh, A. Khodak, J. Klein, E. Kolemen, G. Larsen, R. Majeski, B.J. Merrill, N.B. Morley, G.H. Neilson, B. Pint, M.E. Rensink, T.D. Rognlien, A.F. Rowcliffe, S. Smolentsev, M.S. Tillack, L.M. Waganer, G.M. Wallace, P. Wilson, S.J. Yoon, Critical exploration of liquid metal plasma-facing components in a fusion nuclear science facility, Fusion Sci. Technol. 75 (2019) 886–917.

[3] U. Müller, L. Bühler, Magnetofluiddynamics in Channels and Containers, Springer, Berlin, Heidelberg, 2001.

[4] M.-J. Ni, R. Munipalli, P. Huang, N.B. Morley, M.A. Abdou, A current density conservative scheme for incompressible MHD flows at a low magnetic Reynolds number. Part II: On an arbitrary collocated mesh, J. Comput. Phys. 227 (2007) 205–228.

[5] S. Smolentsev, S. Badia, R. Bhattacharyay, L. Bühler, L. Chen, Q. Huang, H.-G. Jin, D. Krasnov, D.-W. Lee, E.M. de les Valls, C. Mistrangelo, R. Munipalli, M.-J. Ni, D. Pashkevich, A. Patel, G. Pulugundla, P. Satyamurthy, A. Snegirev, V. Sviridov, P. Swain, T. Zhou, O. Zikanov, An approach to verification and validation of MHD codes for fusion applications, Fusion Eng. Des. 100 (2015) 65–72.

[6] V. Dousset, Numerical Simulations of MHD Flows Past Obstacles in a Duct Under Externally Applied Magnetic Field (Ph.D. thesis), Coventry University, 2009.

[7] C. Mistrangelo, L. Bühler, Development of a numerical tool to simulate magneto-hydrodynamic interactions of liquid metals with strong applied magnetic fields, Fusion Sci. Technol. 60 (2011) 798–803.

[8] E.M.D. les Valls, Development of a simulation tool for MHD flows under nuclear fusion conditions (Ph.D. thesis), Universitat Politècnica de Catalunya, 2011.

[9] D. Suarez, A. Khodak, E.M. de les Valls, L. Batet, A formal verification and validation of a low magnetic Reynolds number MHD code for fusion applications, IEEE Trans. Plasma Sci. 50 (2022) 4206–4212.

[10] A. Blishchik, M. van der Lans, S. Kenjereš, An extensive numerical benchmark of the various magnetohydrodynamic flows, Int. J. Heat Fluid Flow 90 (2021) 108800.

[11] S. Siriano, Numerical Simulation of MHD Flows in Breeding Blanket and Plasma-Facing Components (Ph.D. thesis), Sapienza University of Rome, 2022.

[12] C. Greenshields, H. Weller, Notes on Computational Fluid Dynamics: General Principles, CFD Direct Ltd, Reading, UK, 2022.

[13] J. Roenby, H. Bredmose, H. Jasak, A computational method for sharp interface advection, R. Soc. Open Sci. 3 (2016) 160405.

[14] J. Zhang, M.J. Ni, Direct simulation of multi-phase MHD flows on an unstructured cartesian adaptive system, J. Comput. Phys. 270 (2014) 345–365.

[15] S. Siriano, N. Balcázar, A. Tassone, J. Rigola, G. Caruso, Numerical simulation of high–density ratio bubble motion with interIsoFoam, Fluids 7 (2022) 152.

[16] J.U. Brackbill, D.B. Kothe, C. Zemach, A continuum method for modeling surface tension, J. Comput. Phys. 100 (1992) 335–354.

[17] Y. Mori, K. Hijikata, I. Kuriyama, Experimental study of bubble motion in mercury with and without a magnetic field, J. Heat Transfer 99 (1977) 404–410.

[18] K. Jin, P. Kumar, S.P. Vanka, B.G. Thomas, Rise of an argon bubble in liquid steel in the presence of a transverse magnetic field, Phys. Fluids 28 (2016).

[19] H.D. Mendelson, The prediction of bubble terminal velocities from wave theory, AIChE J. 13 (1967) 250–253.

[20] Y. Pan, J. Zhang, Z.-H. Wang, M.-J. Ni, Development of MHD solver based on an adaptive mesh refinement technique, Fusion Eng. Des. 87 (2012) 630–633.

[21] A.Y. Shishko, A theoretical study of steady film flows in a coplanar magnetic field, Magnetohydrodynamics 28 (1992) 170–181.

[22] S. Siriano, A. Tassone, G. Caruso, Numerical simulation of thin–film MHD flow for nonuniform conductivity walls, Fusion Sci. Technol. 77 (2021) 144–158.

[23] K. Hijikata, Y. Mori, Y. Takahasi, Study on a shock wave in liquid metal two–phase mixture with and without magnetic field, Nucl. Eng. Des. 95 (1986) 343–352.
[24] Q. Sun, T. Peng, Z. Zhou, Z. Chen, S. Wang, CFD simulation of pressure wave propagation in the helium coolant tube break accident of DFLL-TBM, Fusion Eng. Des. 136 (2018) 950–957.
[25] L. Melchiorri, S. Siriano, A. Tassone, RELAP5/Mod3.3 MHD module Development and Validation: WCLL-TBM mock-up model, Fusion Eng. Des. (2023) This conference, under review.
[26] C. Mistrangelo, L. Bühler, C. Alberghi, S. Bassini, L. Candido, C. Courtessole, A. Tassone, F.R. Urgorri, O. Zikanov, MHD R&D activities for liquid metal blankets, Energies 14 (20) (2021) 6640.
[27] S. Smolentsev, Modeling of transport processes in liquid-metal fusion blankets: Past, present, and future, Fusion Sci. Technol. 79 (3) (2023) 251–273.
[28] F. Iannone, F. Ambrosino, G. Bracco, M.D. Rosa, A. Funel, G. Guarnieri, S. Migliori, F. Palombi, G. Ponti, G. Santomauro, P. Procacci, CRESCO ENEA HPC clusters: A working example of a multifabric GPFS spectrum scale layout, in: 2019 International Conference on High Performance Computing and Simulation, HPCS 2019, IEEE, 2019, pp. 1051–1052.